

**ANNUAL PROGRESS REPORT
GEORGIA TECH FUSION RESEARCH CENTER**

Assembled by W. M. Stacey
October, 2006

CONTENTS

- I. Edge Pedestal Structure and Transport, p1
- II. Rotation, p8
- III. Neutral Atom Transport and Thermal Instabilities, p8
- IV. Conceptual Design of a Fast, Gas-Cooled Transmutation Reactor with a Tokamak Fusion Neutron Source, p9
- V. Investigation of the Influences of Different Auxiliary Heating Methods on the Density Limit in TEXTOR, p22

COLLABORATIONS

- 1. Member of the DIII-D National Tokamak Facility Team.
- 2. With members of the TEXTOR Tokamak Facility.

I. EDGE PEDESTAL STRUCTURE AND TRANSPORT (W. M. Stacey--Georgia Tech, R. J. Groebner and T. E. Evans—General Atomics, J. D. Callen—Univ. Wisconsin)

The major effort over the past year has been devoted to understanding the structural and transport aspects of the physics of the edge pedestal in H-mode plasmas.

A. *Structure of the Edge Pedestal* (W. M. Stacey)

We have been working to develop an understanding and computational capability for analyzing pedestal structure and transport in between, in the absence of, or averaged over ELMS; i.e. the non-MHD physics of the edge pedestal.

Based on work to date, our current understanding of the cause for the observed pedestal structure is as follows [1]. Conservation of momentum and particles constrains the pressure gradient to balance an inward pinch (primary) and the buildup of the outward particle flux due to ionization of recycling neutrals (secondary). Thus, the pressure gradient scale length, hence the pressure profile, is determined by

$$\frac{-1}{p} \frac{dp}{dr} \equiv L_p^{-1} = (V_{ion} - V_{pinch}) / D \quad (1)$$

where the “pinch velocity” V_{pinch} is a collection of terms given below and V_{ion} is the radial ion velocity which may be determined from the continuity equation. The heat conduction relation

determines the temperature gradient scale length, hence the temperature profile, $L_T^{-1} = (Q - 2.5T\Gamma) / nT\chi$. The temperature profiles can be calculated by integrating

$$\frac{-1}{T} \frac{dT}{dr} = \frac{(Q - 2.5T\Gamma)}{nT\chi} \quad (2)$$

over the edge region, and the density profiles can be calculated by integrating

$$\frac{-1}{n} \frac{dn}{dr} = L_p^{-1} - L_T^{-1} = \frac{(V_{ion} - V_{pinch})}{D} - \frac{(Q - 2.5T\Gamma)}{nT\chi} \quad (3)$$

over the edge region. Note that $\Gamma = nV_{ion}$. The V_{pinch} represents a collection of terms

$$V_{pinch,i} = \frac{\left[-M_{\phi i} - n_i e_i E_{\phi}^A + n_i m_i (\nu_{il} + \nu_{di}^*) \left(f_p^{-1} V_{\theta i} + \frac{E_r}{B_{\theta}} \right) - n_i m_i \nu_{il} V_{\phi l} \right]}{n_i e_i B_{\theta}} \quad (4)$$

arising in the derivation from momentum balance. Here M_{ϕ} is the toroidal component of the beam momentum input, $f_p \equiv B_{\theta} / B_{\phi}$, ν_d^* is the frequency for the radial transport of toroidal angular momentum by viscosity, convection, charge-exchange, etc. (which can be determined from experiment), and the other terms have their usual meaning.

The heat and particle fluxes, $Q(r)$ and $\Gamma(r)$, must be determined by solving the heat and particle balance equations in the edge, taking into account radiation, energy equilibration and the atomic physics associated with recycling neutrals. In H-mode, the observed negative edge peaking in poloidal rotation velocity and radial electric field produce a large inward (negative) pinch velocity. When we take the experimental poloidal and toroidal velocities to evaluate V_{pinch} and take the experimental L_T^{-1} , integration of Eq. (3) leads to edge density profiles that are in agreement with the Thomson density profiles [1].

Thus, the “structure” of the edge pedestal is determined by the above equations. The “width” of the density profile is the region over which the right side of Eq.(3) is large, and the “widths” of the temperature profiles are the regions over which the right side of Eq. (2) are large for the respective species. As the above equations indicate, the temperature and density profiles (the structure) are coupled not only to each other but also to the toroidal and poloidal rotation (and/or radial electric field) profiles (via V_{pinch}).

These results suggest that the description of pedestal structure given by Eqs. (2) and (3), which are nothing more than a rearrangement of the momentum and particle balance equations, should be used to guide the experimental investigation of pedestal structure. This would suggest measuring poloidal and toroidal velocity profiles (for main and impurity ions), making an independent measurement of radial electric field profiles, inferring $\chi_{i,e}^{exp}$ as described below and ν_d^* as described in [1], measuring neutral densities, etc. in the edge region.

The obvious next steps in support of this line of investigation are: 1) to develop a means to determine the ion and electron heat diffusivities in the edge pedestal, which would enable a first-principles calculation of L_T from Eq. (2); and 2) to develop a first-principles calculation for rotation velocities and the radial electric field in the edge pedestal, which would allow a first-principles evaluation of V_{pinch} from Eq. (4), hence of the edge pressure and density profiles calculated from integration of Eqs. (1) and (3), respectively.

B. Inference of Thermal Transport in the Edge Plasma (W. M. Stacey)

We have shown [2] that it is possible to infer χ^{exp} by rearranging Eq. (2),

$$\chi_{i,e}^{\text{exp}}(r) = L_{Ti,e}^{\text{exp}}(r) \left[\frac{Q_{i,e}(r)}{n_{i,e}^{\text{exp}}(r) T_{i,e}^{\text{exp}}} - \frac{5}{2} \frac{\Gamma_{i,e}^{\text{exp}}(r)}{n_{i,e}^{\text{exp}}(r)} \right] \quad (5)$$

using measured n , T and dT/dr , and integrating

$$\frac{\partial \Gamma}{\partial r} = n_e n_o <\sigma v>_{ion} + S_{nb}, \quad \Gamma(r_{sep}) = \Gamma_{sep}^{\text{exp}} \quad (6)$$

where n_o is the density of recycling and gas fueling neutrals and S_{nb} is the source rate of plasma ions due to neutral beam (and pellet) injection, and the heat balance equations

$$\frac{\partial Q_i}{\partial r} = q_{nbi} - \frac{3}{2} (T_i - T_o^c) n_i n_o^c <\sigma v>_{cx+el} - q_{ie}, \quad Q_i(r_{sep}) = Q_{sepi}^{\text{exp}} \quad (7a)$$

and

$$\frac{dQ_e}{dr} = q_{nbe} + q_{ie} - n_e n_o <\sigma v>_{ion} E_{ion} - n_e n_z L_z, \quad Q_e(r_{sep}) = Q_{sepe}^{\text{exp}} \quad (7b)$$

inward from the separatrix to determine the edge distributions of $\Gamma(r)$ and $Q_{i,e}(r)$ needed to evaluate the radial distribution of $\chi_{i,e}$ from Eq. (5). Here $q_{nbi,e}$ is the local neutral beam power deposition density, n_o is the recycling neutral density, n_o^c is the density of ‘cold’ recycling neutrals that have not yet collided inside the separatrix and $1.5T_o^c$ is their average energy, $q_{ie} \sim (T_i - T_e)/T_e^{1.5}$ is the ion-electron equilibration rate, $E_{ion}(T_e, n_e)$ is the ionization energy, n_z is the impurity (carbon) density, $L_z(T_e, n_o)$ is the impurity radiation emissivity, $<\sigma v>_{cx+el}(T_i)$ is the charge-exchange plus elastic scattering rate coefficient, and $<\sigma v>_{ion}(T_e, n_e)$ is the electron impact ionization rate coefficient. The experimental $n_{e,z}$ and $T_{i,e}$ and the calculated neutral density are used to evaluate the terms in Eqs. (6) and (7), which are then integrated radially inward from the experimental separatrix boundary conditions for the particle and heat fluxes.

C. Investigation of thermal transport in edge pedestal in L-mode and H-mode (W. M. Stacey and R. J. Groebner)

The ion and electron thermal diffusivities in the edge region have been inferred from density and temperature profile measurements during the fully developed L-mode stage, during an early transient H-mode stage and during a fully developed H-mode stage of a DIII-D discharge with a long ELM-free H-mode phase. The ion and electron conductive heat flux edge profiles used to evaluate the thermal diffusivities were calculated taking into account radiation, atomic physics effects associated with recycling neutrals, ion-electron collisional equilibration and neutral beam heating in the edge, as outlined above.

The inferred thermal diffusivities for both ions and electrons decreased by about an order of magnitude between the L-mode and ELM-free H-mode stages of the discharge (Figs 1 and 2), as anticipated. This decrease occurred across the entire outer 15% of the plasma minor radius,

not just in the localized regions in the outer 5% where the steep-gradient pedestals in density and temperature formed in the H-mode. There was a broad (width about 5% of minor radius) minimum in χ_e^{exp} centered at about 95% of the minor radius in the H-mode stages, even though the steepness of the measured T_e gradient increased with radius up to within less than 1% of the separatrix.

Comparison of $\chi_{e,i}^{\text{exp}}$ with theoretical predictions found reasonably good agreement in the L-mode stage for the paleoclassical prediction of χ_e and the thermal-instability prediction of χ_i . In the H-mode stages, the broad minimum in the inferred χ_e^{exp} was well under any of the theoretical predictions (paleoclassical, etg, tem, resistive ballooning). The inferred χ_i^{exp} agreed reasonably well with the itg prediction (and not with the neoclassical prediction) of χ_i early in the H-mode stage, but χ_i^{exp} was significantly larger than either of these predictions in the outer 4% of the minor radius later in the H-mode stage. The resistive ballooning mode prediction of χ_i agreed with χ_i^{exp} in magnitude but not in profile over this outer 4% of the minor radius. The electron thermal diffusivity comparison is shown in Figs. 3.

A DIII-D Science Meeting presentation was made on this work, and a paper has been submitted to *Physics of Plasmas* [3].

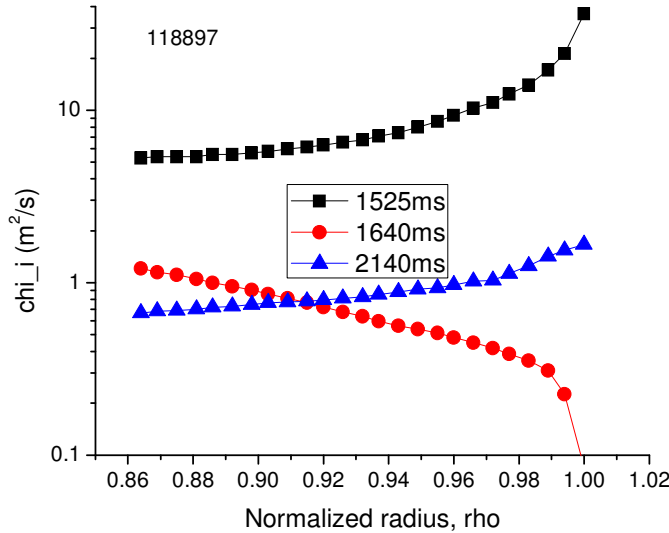


Figure 1. Experimentally inferred ion thermal diffusivity just before L-H (1525ms), just after L-H (1640ms) and well after L-H (2140ms).

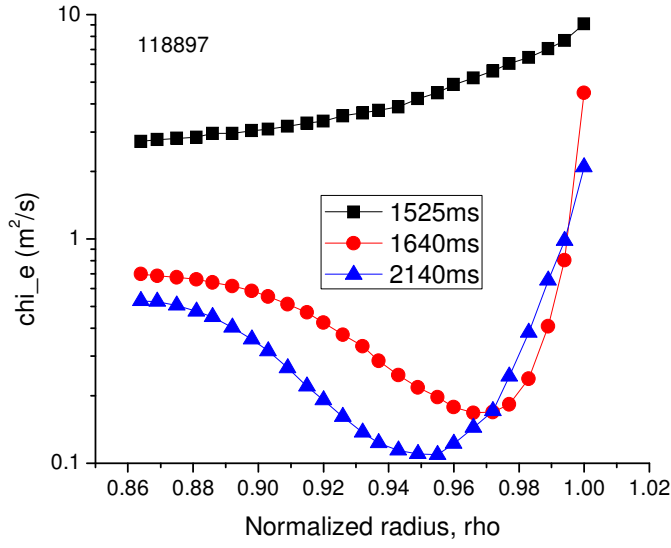


Figure 2. Experimentally inferred electron thermal diffusivity just before L-H (1525ms), just after L-H (1640ms) and well after L-H (2140ms).

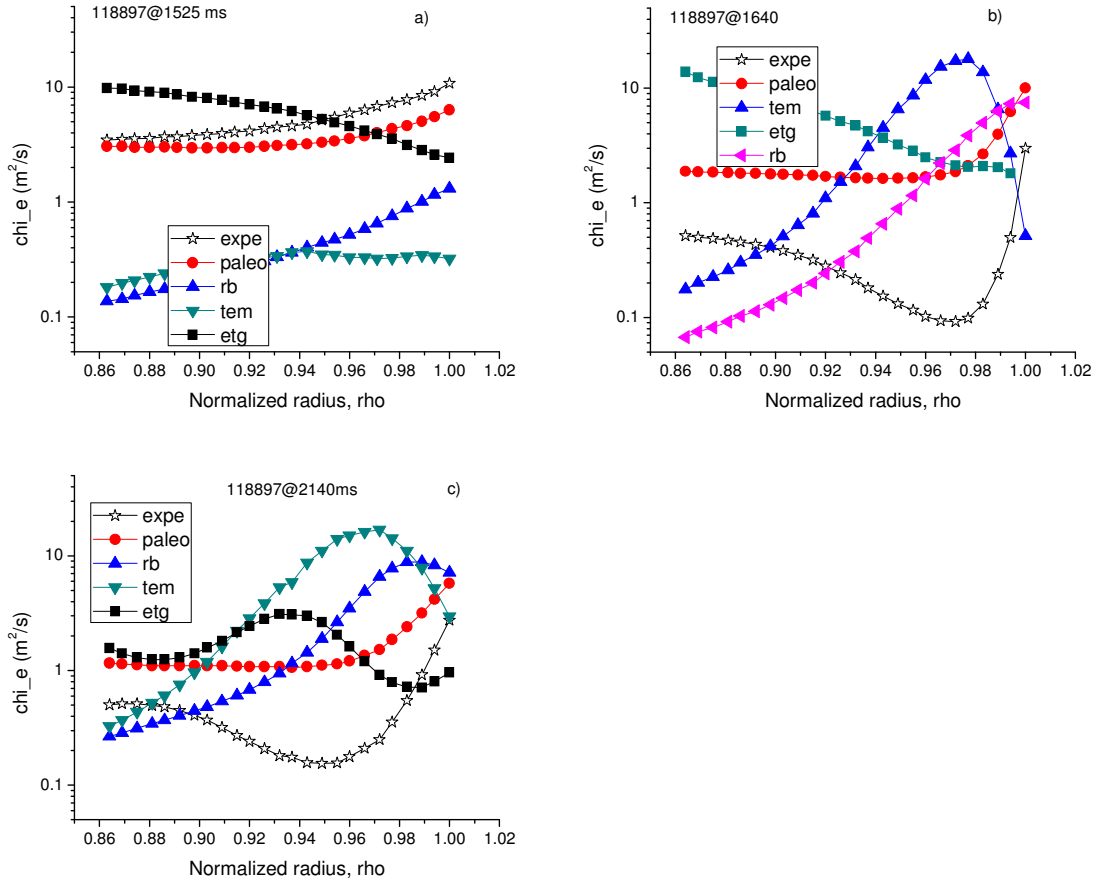


Figure 3. Comparison of experimentally inferred electron thermal diffusivities with theoretical predictions a) just prior to L-H, b) just after L-H, and c) well after L-H. (expe=inferred from exp., paleo=paleoclassical, rb= resistive ballooning mode, tem=trapped electron mode, etg=electron temperature gradient mode)

D. Investigation of edge thermal transport in ELMing and ELM-suppressed H-modes (W. M. Stacey and T. E. Evans)

Following the Science Meeting presentation on the above work, the same type of thermal transport calculations were undertaken for the I-coil ELM suppression experiment. Thermal transport was inferred from experimental temperature and density profiles and calculated conductive flux profiles (taking into account edge cooling due to atomic physics, ion-electron equilibration and convection) in the edge plasma for a matched pair of H-modes, one ELMing and the other with ELMs suppressed by resonant magnetic perturbations. The inferred thermal diffusivities were compared with the predictions of various theoretical models.

Both χ_i^{exp} and χ_e^{exp} increase with time between ELMs, most strongly just inside the separatrix. Evidently, some transport mechanism(s) increases in strength as the pedestal pressure builds up between ELMs, but is suppressed by the ELM event.

The resonant magnetic perturbations introduced by the I-coil do increase χ_e^{exp} (relative to the background value without the I-coil just after the ELM crash), as predicted theoretically. Remarkably, this increased χ_e^{exp} due to the I-coil is well matched over the entire edge region to the χ_e^{exp} just before the ELM crash in the ELMing H-mode (Fig. 4), which would seem to indicate that it is not the increase in χ_e^{exp} caused by the resonant magnetic field perturbations that suppresses the ELMs. Rather, the resonant magnetic perturbation seems to cause the discharge to operate at a lower average and pedestal density and thus at a pedestal pressure below the ELM threshold.

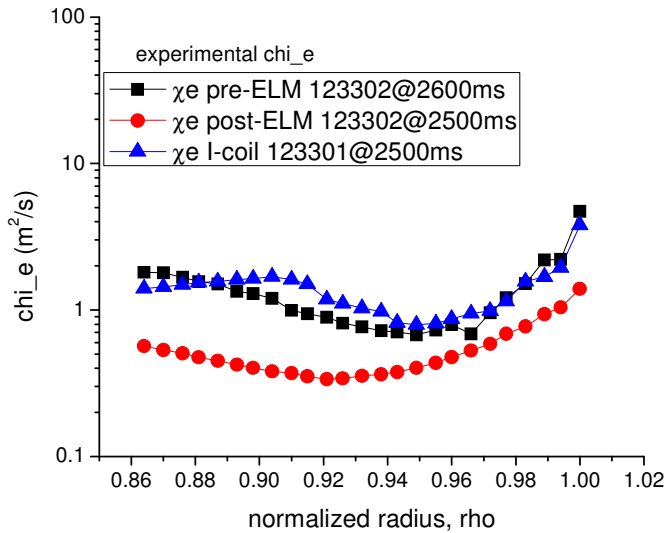


fig 14

Figure 4. Comparison of χ_e^{exp} in ELMing and ELM-free shots.

None of the theoretical predictions provides a good fit to the experimentally inferred thermal diffusivity over the entire edge region. The inferred χ_i^{exp} profile agrees best with its predictions, although there is a significant under-prediction just inside the separatrix for which there must be another explanation. The experimentally inferred χ_e^{exp} agrees best with the paleoclassical and the magnetic perturbation diffusion predictions for the ELM-suppressed discharge and with the paleoclassical prediction just prior to the ELM crash in the ELMing discharge.

A DIII-D Science Meeting presentation was made on this work, and a paper for *Physics of Plasmas* [4] has been submitted.

E. *Comparison of Paleoclassical Theory with Inferred Electron Thermal Diffusivity* (W. M. Stacey and J. D. Callen)

The paleoclassical transport model for electron thermal diffusivity of J. D. Callen (UWisconsin) was implemented into the data analysis code for comparison with the inferred electron thermal diffusivity in DIII-D in the edge of DIII-D. Several calculations were made in support of a broad evaluation of the paleoclassical theory [5].

F. *Effect of Rotation and Radial Electric Field* (W. M. Stacey)

As discussed above, analysis of the momentum balance relations indicates that the rotation velocity and radial electric field profiles that enter the “pinch velocity” largely determine the pedestal structure (pressure and density profiles and widths). A theoretical formalism for calculating the rotation velocities and radial electric field inside the separatrix has been developed [6], but not yet implemented.

We note that theoretical extensions of the rotation theory are needed for application in the edge plasma, primarily extensions to gyroviscosity for the steep-gradient plasma edge, but also extensions to relate the electric field and flow inside the separatrix to the flow and electrostatic potential structure outside the separatrix in the SOL and divertor. We will propose to undertake such a theoretical development in the coming year. This development may well also shed some light on the large rotation velocities that are measured outside the separatrix.

We propose to continue analyzing edge pedestal structure data in DIII-D, making use of this new capability to calculate rotation and radial electric field profiles. This line of investigation should provide new insights as to the mechanisms controlling the edge pedestal in between and in the absence of ELMs.

Recent Publications on Edge Pedestal Structure and Transport

1. W. M. Stacey and R. J. Groebner, “Investigation of edge pedestal structure in DIII-D”, *Phys. Plasmas*, 13, 012513 (2006).
2. W. M. Stacey and R. J. Groebner, “Thermal transport in the DIII-D edge pedestal”, *Phys. Plasmas*, 13, 072510 (2006).
3. W. M. Stacey and R. J. Groebner, “Thermal transport analysis of the edge region in the low and high confinement stages of a DIII-D discharge”, *Phys. Plasmas*, submitted (2006).
4. W. M. Stacey and T. E. Evans, “Investigation of background edge thermal transport in ELMing and ELM-suppressed H-modes in DIII-D”, *Phys. Plasmas*, submitted (2006).
5. J. D. Callen, ..., W. M. Stacey, ..., “Experimental Tests of Paleoclassical Transport”, IAEA presentation, to be submitted to *Nucl. Fusion* (2006).
6. W. M. Stacey, “Rotation velocities and the radial electric field in the plasma edge”, *Contrib. Plasma Phys.*, 46, 597 (2006).

II. ROTATION (R. W. Johnson, W. M. Stacey, J. Mandrekas—Georgia Tech)

We have recently completed a comparison of neoclassical rotation calculations with toroidal rotation measurements in several DIII-D shots in different energy confinement regimes (L-mode, ITB, H-mode, QDB) [1]. We over-predicted the measured carbon toroidal rotation velocity profiles by well less than a factor of 2, indicating that neoclassical gyroviscosity can account for more than 50% of the radial transport of toroidal angular momentum in DIII-D shots in a wide range of energy confinement regimes. (An exception is the QDB shots, in which the large Cu and Ni concentrations invalidate the non-inherent “2-species” assumption of our present model, and for which the over-prediction is about a factor of 3.) It remains to be seen whether this over-prediction is associated with imperfections in the calculation model or experimental measurement (e.g. the recent atomic physics correction to the rotation measurements increase the measured toroidal rotation by 10%, which presumably would reduce by that amount our over-prediction) or indicates the presence of additional transport mechanisms. A paper [1] summarizing the theory and documenting the comparison with experiment has been published.

We have not yet undertaken a comparison with poloidal rotation measurements, because of the large uncertainty that generally was felt to be associated with them, even though the poloidal rotation calculation is part of our calculation of the gyroviscous momentum transport coefficient. Now that the atomic physics correction has been developed and there is more confidence in the measured poloidal velocity, we have initiated an analysis of some of the rotation data to which the correction has been applied.

A talk on the rotation calculation was given at a DIII-D Integrated Modeling Meeting in summer 2006, for the purpose of exploring ways that our calculation could be incorporated into codes used in DIII-D analysis as well as to report our recent results. Basically, the present nonlinear equation solving routine that is used to solve the rotation equations could be incorporated as a post-run option in ONE-TWO or it could be made available as a stand-alone code, in either case needing some automation of experimental input.

The calculational procedure for the toroidal and poloidal rotation profiles using neoclassical momentum transport [1] has been extended from two to a multiple number of ion species. A symbolic algebra routine has been applied to rederive the rotation equations through higher order in $\varepsilon \equiv r/R$ than was retained previously [1]. The previous derivation was confirmed through leading order in ε . The procedure for assembling input data has been streamlined, allowing for the analysis of any shot for which a TRANSP analysis has been performed. New solver routines for the non-linear rotation equations have been investigated. This new formulation of the rotation calculation procedure is being debugged at present.

Recent Publications on Plasma Rotation

1. W. M. Stacey, R. W. Johnson and J. Mandrekas, “A neoclassical calculation of toroidal rotation profiles and comparison with DIII-D measurements”, Phys. Plasmas, 13, 062508 (2006).

III. NEUTRAL ATOM TRANSPORT AND THERMAL INSTABILITIES

(D. K. Zhang, W. M. Stacey, J. Mandrekas, Z. W. Friis—Georgia Tech)

We have previously introduced (Nucl. Fusion, 34, 1385, 1994), developed and validated, implemented into the GTNEUT code (Computer Phys. Commun., 161, 36, 2004) and benchmarked against Monte Carlo calculations and measurements in DIII-D (Nucl. Fusion, 43, 314, 2003; Phys. Plasmas, 13, 062509, 2006) a fast and accurate 2D neutral transport calculation which can achieve comparable accuracy as Monte Carlo with several orders of magnitude less computing time. With the improved approximations developed in the PhD thesis of D-K. Zhang and published this year [1,2] the computational accuracy has become essentially the same as

Monte Carlo. This computational efficiency raises the possibility that 2D neutral recycling calculations could be run routinely in experimental analysis.

The required geometry input for GTNEUT can be provided by a UEDGE geometry file or by hand. Background plasma density and temperature distributions and the neutral sources must also be provided as input. In order to realize the potential of GTNEUT being run routinely in experimental analysis it would be necessary to automate the provision of this geometrical and background plasma and neutral source input.

A practical possibility is to automate a ‘generic’, perhaps simplified, geometry input generator for the experimental configuration (DIII-D in our case), to make use of a combination of experimental data and “simple” SOL-divertor plasma models such as Stangeby’s “onionskin” model or our “integrated core/2-point/2D neutrals” model for providing the background divertor plasma parameters, and to use core power and particle balances and experimental data to calculate (iteratively) heat and particle fluxes out of the core into the SOL. (The present “integrated core/2-point/2D neutrals” code works like this but with a hardwired, simplified geometry neutral transport model based on the same methodology used in GTNEUT.)

A talk on the GTNEUT code and the comparison calculations with Monte Carlo for DIII-D neutrals measurements was presented at a DIII-D Integrated Modeling Meeting in summer 2006. The options for making use of GTNEUT in DIII-D analyses and for automating the input preparation were discussed there and elsewhere. Several members of the DIII-D Team appreciate the potential value of a fast neutral transport code with the geometric capability of GTNEUT for investigating various neutrals-related problems., and several possibilities for coupling GTNEUT with plasma edge codes such as UEDGE or B2.5 were discussed. However, the most likely option for using GTNEUT for routine DIII-D analyses would appear to be to use it to replace the present simplified geometry 2D neutrals code in our “integrated core/2-point/2D neutrals” code. Since models for thermal instabilities (MARFES, radiative collapse, etc.) and pedestal structure and transport are part of this code, this would have the added advantage of making these calculations more widely available for DIII-D analysis.

Recent Publications on Neutral Atom Transport and Thermal Instabilities

1. D.K. Zhang, J. Mandrekas and W. M. Stacey, “Higher order approximations of the transmission and escape probability method for neutral particle transport in edge plasmas”, *Phys. Plasmas*, 13, 062509 (2006).
2. D.K. Zhang, J. Mandrekas and W. M. Stacey, “Improvements in the 2D TEP Neutral Particle Transport Calculation in Edge Plasmas”, *Contrib. Plasma Phys.*, 46, 570 (2006).
3. W. M. Stacey, “A Survey of Thermal Instabilities in Tokamak Plasmas”, *Fusion Sci.&Tech.*, to be published (2006).

IV. CONCEPTUAL DESIGN OF A FAST, GAS-COOLED TRANSMUTATION REACTOR WITH A TOKAMAK FUSION NEUTRON SOURCE

(W. M. Stacey, K. A. Boakye, S. K. Brashear, A. C. Bryson, K. A. Burns, E. J. Bruch, S. A. Chandler, O. M. Chen, S. S. Chiu, J-P. Floyd, C. J. Fong, S. P. Hamilton, P. B. Johnson, S. M. Jones, M. Kato, B. A. MacLaren, R. P. Manger, B. L. Merriweather, C. Mitra, K. R. Riggs, B. H. Shrader, J. C. Schulz, C. M. Sommer, T. S. Sumner, J. S. Wagner, J. B. Weathers, C. P. Wells, F. H. Willis, Z. W. Friis, J. I. Marquez-Danian, R. W. Johnson, C. de Oliveira, H. K. Park, and D. W. Tedder—Georgia Tech)

The concept of a sub-critical fast transmutation reactor based on nuclear and separations technologies being developed in the GEN-IV¹ and AFCI² initiatives and using a D-T tokamak fusion neutron source based on ITER physics and technology²⁷ has been developed in a series of studies⁷⁻¹⁵ at Georgia Tech over the past several years. The general design objective was a 3000

MWth, passively safe, sub-critical fast reactor driven by a fusion neutron source that could fission the TRU in the SNF discharged annually by three 1000 MWe LWRs. The general fuel cycle objective was $> 90\%$ burnup of this TRU (in order to reduce the HLWR requirements by an order of magnitude relative to the present once-through LWR fuel cycle) while minimizing the nuclear fuel reprocessing steps. The designs were constrained to use ITER physics and technology²⁷ for the fusion neutron source, to use nuclear and reprocessing technology being evaluated in the GNEP/AFCI/GEN-IV studies, to use extensions of existing nuclear fuel technology but with TRU, and to achieve tritium self-sufficiency for the fusion neutron source.

A. *The FTWR and GCFTR Studies*

Sub-critical transmutation reactors based on two of the nuclear technologies being developed in the GEN-IV studies have been examined. The Fusion Transmutation of Waste Reactor (FTWR) series of studies was based on a variant of the Lead Cooled Fast Reactor and the Sodium Cooled Fast Reactor in the GEN-IV initiative--a fast-spectrum reactor using a metal fuel consisting of TRU alloyed with zirconium in a zirconium matrix and cooled by a liquid metal (Li17Pb83 eutectic), which also served as the tritium breeder. The Gas Cooled Fast Transmutation Reactor (GCFTR) series of studies was based on a variant of the Gas Cooled Fast Reactor in the GEN-IV initiative--a fast-spectrum reactor using TRU-oxide fuel in coated TRISO particle form in a SiC matrix cooled by He. Both the FTWR and GCFTR cores are annular and located outboard of the toroidal plasma chamber. The core plus plasma chamber were surrounded first by a reflector (tritium breeding blanket for GCFTR) and then by a shield to protect the magnets from radiation damage and heating, as indicated in Fig. 1 for the GCFTR design.

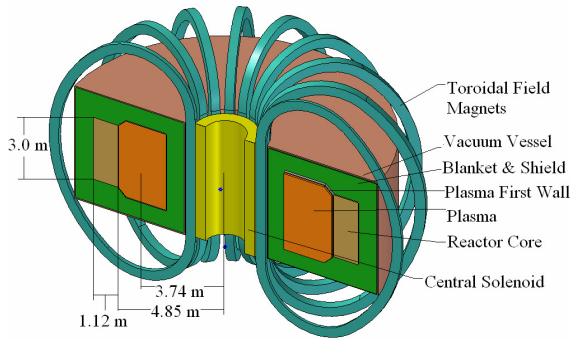


Fig. 1 Gas Cooled Fast Transmutation Reactor

The ANL metal fuel, liquid metal cooled reactor design²⁸ was adapted to accommodate Pb-Li eutectic coolant and TRU-Zr fuel for the FTWR designs. The fast, He-cooled reactor designs being developed under the GEN-IV Program guided the choice of the GCFTR core design, and the coated fuel particle technology being developed in the NGNP program²⁹ was adapted for TRU-oxide fuel for the GCFTR. Tritium breeding was accomplished in the Pb-Li coolant in the FTWR designs and in a Li_2O blanket surrounding the plasma and reactor core in the GCFTR designs.

The fusion technology was based on the ITER design²⁷. The superconducting magnet design was based directly on the ITER cable-in-conduit design scaled down to maintain the same stress level. The first-wall and divertor designs were adapted from the ITER design to accommodate the different coolants. An Lower-Hybrid-Resonance heating and current drive system was adapted from ITER.

B. Transmutation Reactor Cores

FTWR

The fuel is a transuranic zirconium alloy (TRU-10Zr) dispersed in a zirconium matrix in pin form and clad with a ferritic steel similar to HT-9. The relative amounts of transuranics and zirconium in the fuel region are adjusted to achieve the desired neutron multiplication ($k_{\text{eff}} = 0.95$) at the beginning of each burn cycle. At equilibrium, the transuranics will constitute approximately 45% of the fuel volume. The annular transmutation reactor core is outboard of the plasma, and both are surrounded by reflector and shield (Fig. 1). The design of the FTWR transmutation reactor is based on the ANL ATW blanket design studies²⁸. The same pin and assembly geometry was used, with the exception that the length of the assembly was increased to 228 cm. Table II gives the basic data for the fuel assembly design. The reactor core is 40 cm thick and consists of 470 assemblies, 1/5 of which will be ‘half assemblies’ placed in the gaps along the interior and exterior surfaces of the reactor region to produce a more uniform annular distribution. For 3000 MW_{th} total reactor power uniformly distributed in the fuel pins, the volumetric heat source is $q''' = 42.2 \text{ MW/m}^3$. The main coolant parameters are given in Table I. The required pumping power is 130 MW, the majority of which is needed to overcome MHD losses.

Table I Core and Fuel Assembly Parameters

	FTWR	GCFTR
Core in radius, cm	500	485
Core width, cm	40	112
Core height, cm	228	300
Pin Diameter, cm	0.635	1.526
Pins per assembly	217	384
Assy. Flat to Flat, cm	16.1	36.6
Assy. Length, cm	228	300
Assemblies in Core	470	245
Core Cool Flow, kg/s	51630	3280
Coolant $T_{\text{in}}/T_{\text{out}}$, °K	548/848	553/767
Materials Fuel	20	60
(v/o) Structure	10	10
Coolant	70	30

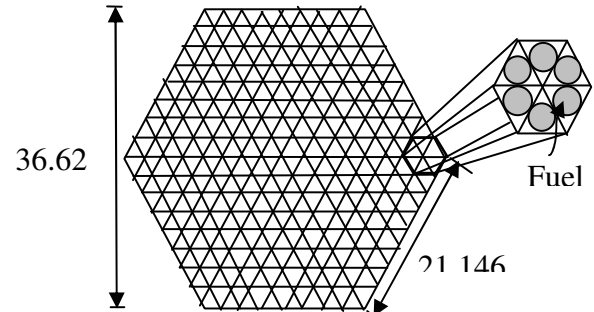


Figure 2 GCFTR Fuel Assembly

GCFTR

Design concepts were developed for several TRISO (tri-material isotropic) and BISO (bi-material isotropic) particles. These particles are embedded in a SiC matrix, then formed into a fuel pin clad with ODS steel, as indicated in Table I. Nominal thermal parameters are given in Table I. A He coolant v/o $\geq 25\%$ would be adequate for heat removal under normal operating conditions.

A cross-section of the fuel assembly for the GCFTR is shown in Fig. 2.

The materials composition for the two reactor types are given in Table II.

A. Fuel Cycle Analyses

The great advantage of sub-critical operation is the variety of transmutation fuel cycles that it makes available, some of which are examined in this section. The composition changes in the fuel cycle were calculated with the ORIGEN burnup code¹⁷ and the REBUS fuel cycle code¹⁸.

Table II Materials Composition of FTWR and GCFTR

Component	FTWR	GCFTR
Reactor		
Fuel	TRU-Zr metal in Zr matrix	TRU-oxide TRISO, SiC matrix
Clad/structure	FeS/FeS	ODS/ODS
Coolant	LiPb	He
Trit. Breeder	LiPb	Li ₂ O
Reflector	FeS, LiPb	ODS, He, Li ₂ O
Shield	FeS, LiPb, B ₄ C, ZrD ₂ , W	ODS, HfC, Ir, Cd, WC, B ₄ C, He
Magnets	NbSn, NbTi/He (OFHC/LN ₂)	NbSn/He
First-Wall	Be-coated FeS, LiPb	Be-coated ODS, He
Divertor	W-tiles on Cu-CuCrZr, LiPb	W-tiles on Cu – CuCrZr, He

In the FTWR reference fuel cycle¹³ the fuel will remain in the reactor for 5 burn cycles of 564 days each and then be reprocessed, blended with 'fresh' SNF and fabricated into new fuel elements for re-insertion into a FTWR. The fuel will be “shuffled” to a new location in the reactor after each burn cycle and removed for reprocessing after the fifth burn cycle. The fusion neutron source (power level) will be increased from BOC (beginning of cycle) to EOC (end of cycle) to offset reactivity loss and maintain a constant fission power level.

A first generation FTWR operating at 3000 MWt will process approximately 74 MT of transuranics from LWR SNF, of which approximately 56% will be fissioned, 0.2% will be lost to the waste streams, and 44% will be recycled in a second generation FTWR. The second and subsequent generations of FTWRs will use the fuel from the previous generation FTWRs and therefore operate in the equilibrium mode shown in Table III over their entire life.

Table III: An Equilibrium 5-Batch Reprocessing Fuel Cycle for 3000 MWt TRU Fueled FTWR (23 MT Initial TRU Load)¹³

Burn cycle, d	564
5-batch residence, y	7.7
TRU burn/residence, %	29
SNF disposed, MT/yr	101
Fast fluence/residence, 10 ²³ n/cm ²	3.4
BOC k _{eff}	0.925
EOC k _{eff}	0.836
BOC P _{fus} , MW	61
EOC P _{fus} , MW	150

Table IV: An Equilibrium 5-Batch Reprocessing Fuel Cycle for 3000 MWt TRU Fueled GCFTR (37 MT Initial TRU Load)¹¹

Burn cycle, d	376
5-batch residence, y	5.2
TRU burn/residence, %	15.3
SNF disposed, MT/yr	98
Fast fluence/residence, 10 ²² n/cm ²	3.9
BOC k _{eff}	0.936
EOC k _{eff}	0.900
BOC P _{fus} , MW	122
EOC P _{fus} , MW	199

Repeated recycling of the discharged transuranics from FTWRs in successive generations of FTWRs will ultimately result in the destruction of up to 99.4% of the transuranics discharged from LWRs. At equilibrium, each 3000 MWt FTWR would be able to process the TRU discharged from three

3000 MWt conventional LWRs, so that it is possible to envision a fleet of conventional and transmutation reactors in the thermal power ratio 3/1.

A similar reprocessing fuel cycle was developed for the GCFTR, as indicated in Table IV. However, the emphasis in the GCFTR studies was achieving > 90% burnup of the TRU in the coated fuel particles *without reprocessing* and then removing the > 90% depleted fuel from the reactor and directly depositing it in a HLW repository. Leaving the highly depleted fuel, together with the accumulated fission products in the reactor long enough to achieve such deep burnup would lead to a much less reactive core (e.g. lower multiplication factor, k). The results in Table IV are indicative of the burnup (about 15%) that can be achieved without reprocessing and with $P_{fus} \leq 200$ MW.

By increasing the limit on the fusion neutron source from 200 to 500 MW it is possible to extend the allowable reactivity decrement due to burnup and accumulation of fission products, hence to increase the length of the burn cycle. Several 5-batch, “once-through”, non-reprocessing fuel cycles in which the reactivity decrement associated with fuel burnup was compensated by an increase in neutron source strength to obtain a longer burn cycle length are summarized in Table V. A 400 MW fusion neutron source enables achievement of a 5-batch, 2400 day burn cycle, fuel cycle in a 3000 MWt GCFTR, which is sufficient to obtain > 90 % TRU burnup without reprocessing.

More efficient utilization of the energy content of uranium not only requires that the TRU in SNF discharged from conventional LWR reactors be recovered and fissioned, but that some fraction of the > 99% of natural uranium that is ^{238}U be transmuted to ^{239}Pu and subsequently fissioned. Two possible steady state fuel cycles for a GCFTR fueled with a mixture of 70% ^{238}U and 30% TRU in oxide form are shown in Table VI. A 3000 MWt GCFTR with a 500 MWt fusion neutron source could achieve > 75% utilization of the energy content of uranium (as compared to the present < 1%).

Table V: Once-Through Steady-State 5-Batch Non-Reprocessing Fuel Cycles for 3000 MWt TRU Fueled GCFTR (37 MT Initial TRU Load)¹¹

Burn cycle, d	600	1200	1800	2400
5-batch residence, y	8.2	16.4	24.7	32.9
TRU burnup, %	24.9	49.7	72.4	93.7
SNF disposed, MT/yr	101	101	98	95
Fast Fluence, 10^{23} n/cm ²	0.7	1.3	3.0	4.3
BOC k_{eff}	0.987	0.917	0.856	0.671
EOC k_{eff}	0.927	0.815	0.714	0.611
BOC P_{fus} , MW	13	83	144	329
EOC P_{fus} , MW	73	185	286	389

Table VI: Once-Through Steady-State 5-Batch Non-Reprocessing Fuel Cycles for 3000 MWt 30%TRU-70% ^{238}U Fueled GCFTR (37 MT Initial TRU + ^{238}U Load)¹⁴

Parameter		
Burn cycle, d	600	1800
5-batch residence, y	8.2	24.7
TRU+ ^{238}U burnup, %	24.9	72.4
Fast fluence, 10^{23} n/cm ²	1.2	4.4
BOC k_{eff}	0.590	0.577
EOC k_{eff}	0.576	0.534
BOC P_{fus} , MW	410	423
EOC P_{fus} , MW	424	466

D. Component Lifetimes

The design lifetime of the FTWR and GCFTR neutron source is 40 years at 75% availability, or 30 EFPY. The superconducting magnets are shielded to reduce the fast neutron fluence to the superconductor and the rad dose to the insulators below their respective limits— 10^{19} n/cm² fast neutron fluence for Nb³Sn and 10^9 rads for organic insulators (10^{10} rads for ceramic insulators). The first-wall of the plasma chamber and the plasma-facing part of the divertor will accumulate fast neutron fluences of 7.5 and 5.8×10^{23} n/cm², respectively, over the 30 EFPY lifetime. The radiation damage limit of the ferritic or ODS steel first-wall structure is estimated to be $1.5\text{--}3.0 \times 10^{23}$ n/cm², which implies that it will be necessary to replace the first-wall 2-4 times over the 30 EFPY lifetime. Erosion of the divertor by the incident plasma ion flux will necessitate several replacements over the 30 EFPY lifetime.

The achievement of the fuel cycles discussed above of course is contingent on the reactor fuel and structure radiation damage lifetimes. The FTWR fuel cycle would accumulate a fast neutron fluence of 3.4×10^{23} n/cm² over a 5-batch residence time, which is at the upper limit of the estimated lifetime fluence for the ferritic steel cladding and assembly structure. The fuel would then be reprocessed, re-clad, recycled and placed into a new structural assembly. The similar reprocessing fuel cycle for the GCFTR would accumulate a fast neutron fluence of 3.9×10^{22} n/cm² over a 5.2 year residence time, while the non-reprocessing GCFTR fuel cycles of Table VI would accumulate up to 4.3×10^{23} n/cm². Unfortunately, there is little data for TRISO particles in fast spectra.

E. Fuel Design, Fabrication and Reprocessing for GCFTR

The TRISO coated fuel particle embedded in a SiC matrix in clad fuel pins was chosen as the reference fuel form. A multifaceted study of this fuel form has been conducted. A new TRISO fuel particle was designed with the objective of long lifetime in a fast neutron fluence, and comparison of possible clad materials was made. Fabrication and reprocessing procedures for the TRISO particle were developed.

Fuel Particle Design

The pyrolytic carbon used in normal thermal reactor TRISO particles contracts under irradiation at a rate proportional to neutron energy²⁶, therefore, alternate outer layer materials were considered. Predicted pressures due to fission gas in the buffer were calculated using element concentrations obtained with ORIGEN¹⁷ and the assumption that the gases are ideal at the operating temperature of 942 K. The stresses on the particle's walls were calculated using expressions for a thin-walled pressure vessel. The particle's size was optimized to minimize stress. It was assumed that the first coating layer could be ignored in the initial optimization because it provides little structural support³⁰.

Tungsten carbide (WC) was selected as a replacement in two layers for pyrolytic carbon (PyC) due to concerns over the contraction of PyC in a fast flux²⁶. The thicknesses of the buffer, inner WC, SiC, and outer WC layers were optimized to be 73, 10, 67, and 15 μm , respectively, as shown in Fig. 3. Pressure values were calculated at the nominal operating temperature and for a fuel kernel diameter of 330 μm . The pressure in SiC due to gaseous fission products reached 85.4 MPa with 90% burnup. The corresponding maximum pressure in the outer WC was 157.4 MPa. These values are significantly below the materials' respective UTS values of 200 and 344 MPa. At nominal operating temperature, the particle should not fail due to fission gas buildup at 90 % burnup.

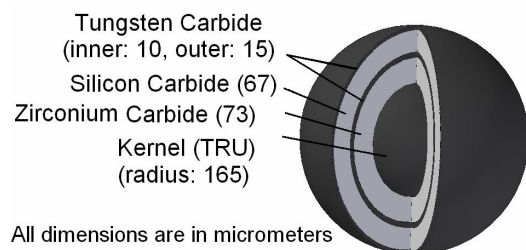


Figure 3: TRISO Fuel Particle

Cladding Material

Alternative cladding materials were examined because the originally chosen⁹ Zircalloy-4 clad swells extensively in a fast flux²⁶. Consultations and literature reviews were the basis of an examination of the possibility of using silicon carbide or a steel as a cladding material. The cladding material study resulted in the choice of an oxide dispersion strengthened steel would make a suitable replacement for Zircalloy-4. The high operating temperature capability of the steel and its resistance to swelling³¹ make it a popular choice in fast reactors. SiC potentially has even more promising qualities, but its database is insufficient to support its near-term use as a cladding in a fast neutron flux.

Fabrication Process

A thorough study was done to determine the best fuel fabrication process for the recommended particle size and composition. Existing technologies were updated to accommodate demands of the designed particle. The fabrication process study yielded a plan for the processes and infrastructure that differ from those previously designed for the fabrication of TRISO particles, and the suggestion that a carbide fuel kernel may be more desirable than the proposed oxide kernel. The proposed fabrication process is outlined in Fig. 4.

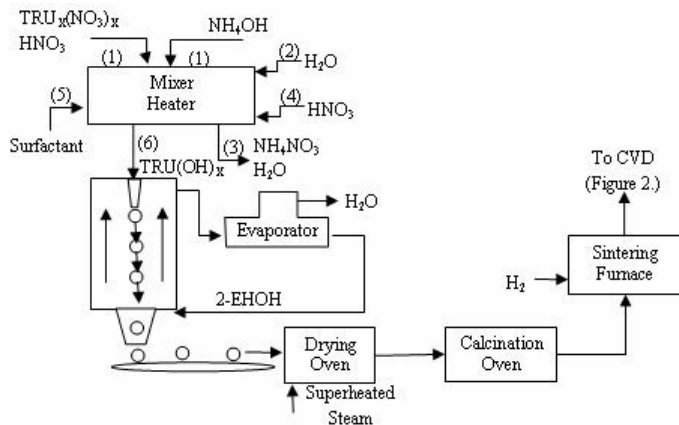
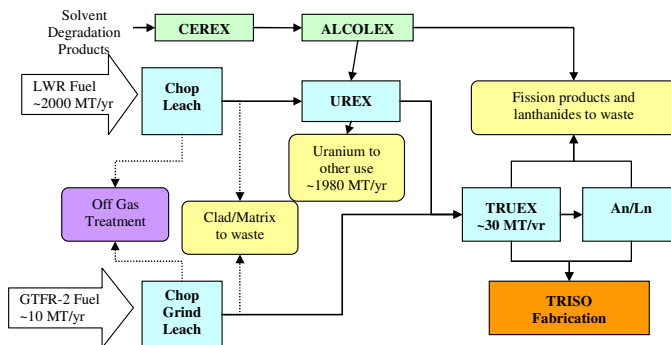


Figure 5: TRISO Particle Reprocessing

Figure 4: TRISO Particle Fabrication



Reprocessing

Reprocessing methods based on currently available UREX/TRUEX technology³²⁻³⁴ were chosen to treat the materials which would be present in the fuel at steady state. Reprocessing the TRISO particle by grinding it down and then using a UREX/TRUEX process was judged feasible, but difficult. The flow sheet is given in Fig. 5.

F. Thermal analysis

The first objective of the GCFTR-3 thermal analysis involved analyzing a loss of coolant accident (LOCA), which entailed determining the decay heat curve. The next objective was the design of an Emergency Core Coolant System (ECCS) which can accommodate this decay heat. During nominal core operation, a thermal analysis of the fuel pin was made in order to find the mass flow-rate of the helium coolant and the required pumping power. Finally, a direct cycle secondary power conversion system was designed.

The core is an annular ring of inner radius 4.85 m, width 1.1 m and height 3 m that surrounds the toroidal plasma neutron source. TRU-oxide fuel in TRISO particles are embedded in a SiC matrix clad with ODS steel in pins. The fuel pin design consists of three layers: an inner TRISO particle layer, a helium gas-filled gap layer, and a ODS (HT-9 properties) steel cladding layer. The pins have a diameter of 1.34 cm and a pitch of 1.8 cm. The fuel/He/structure v/o was 60/30/10. The power density was 42.2 MW/m³ and the thermal output was 3000 MW.

A thermal analysis of the core was performed under severe LOCA conditions--complete loss of normal core cooling. It was assumed that the neutron source was immediately shut down and that all heat addition came from decay heat, which was calculated using the ORIGEN-S¹⁷ code at a burnup of 3000 days with a fuel composition of 30% U-238/ 70% TRU. The initial decay heat represented 8.8% of total thermal output, falling to 2.4% after one hour.

Once coolant is lost, the only significant process for removing heat is through thermal radiation transfer. The results of a sophisticated computation of a LOCA in the annular core of a helium cooled Prismatic Fueled Reactor (PFR)³⁵ were scaled according to surface area and temperature to obtain values for the amount of heat rejected from the core by radiation in the GCFTR-3. Using the mass, specific heat, and scaled rejection heat of the reactor core, the temperature change of the clad was calculated, as shown in Fig.6. The clad inner temperature peaks at 2736K well above the melting point of the clad material (1600K) and the fuel (2300K).

An accumulator system was designed to provide emergency core cooling. The accumulator design was a ring header in the shape of a torus, which was located beneath the core. Attached to the torus were 24 55m³ standby helium tanks. The torus is connected to the reactor via four 6 inch inner diameter injection headers, each containing a flow restrictor and check valve in series, and the entire system was pressurized to 6MPa. The effectiveness of the accumulator is shown in Fig. 6.

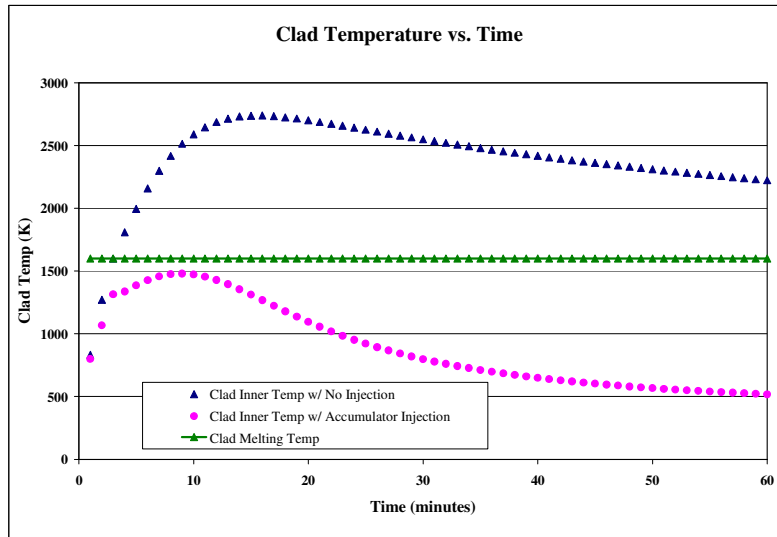


Figure 6 Accumulator effect on cladding temperatures following LOCA

In order to find the mass flow rate of helium coolant under normal operation, a thermal circuit³⁶ was utilized with 33% of the melting temperature of SiC as the limiting factor. The resulting mass flow-rate was 3280 kg/s, corresponding to a specific heat capacity of 5.193×10^3 J/kg-K. A pumping power of 0.172 MW is required to drive the helium at a velocity of 94 m/s.

A Brayton cycle³⁷ was selected for the secondary system. The thermal power produced is 3000MW, with an electrical output of 1020 MW. Taking into account power requirements to run the GCFTR, the net electrical power produced would be ≈ 700 MWe. The temperature in the hot leg is 573 K. Past the compressor the fluid is 767 K at 7 MPa. After leaving the turbine, the temperature is 395 K and the pressure is 2.4 MPa. After the cooler, a state of 424 K and 7 MPa is fed back into the cold leg.

G. Nuclear Analysis

The core is an annular ring of inner radius 4.85 m, width 1.1 m and height 3 m that surrounds the toroidal plasma neutron source. Twenty degree (azimuthal) segments are vacant on opposite sides of the core to allow ports for bringing power into the plasma. The core and surrounding blanket-shield was modeled with a multi-dimensional spherical harmonics code, EVENT¹⁶, and with two continuous energy Monte Carlo codes—MCNP³⁸ and KENO³⁹. Three EVENT models were used $-(x-y)$, $(r-z)$, 3-D. The fusion plasma neutron source was modeled as a uniform 14 MeV source in the plasma region, and the plasma had no further effect on the core neutronics.

Calculations were made 1) to examine the range of k_{eff} that might be expected during core operation, 2) to investigate the power distributions and neutron spectra in core and tritium blanket regions, 3) to evaluate Doppler temperature coefficients and coolant voiding reactivity worth, and 4) to design of the core, tritium breeding blanket and shield.

The core contained 37 MT of TRU-oxide fuel in TRISO particles embedded in a SiC matrix clad with ODS steel in pins with $d=1.34$ cm. The fuel/He/structure v/o was 60/30/10. A 15 cm thick tritium breeding blanket-Li₂O pins cooled by He--surrounded the core and plasma chamber, followed by a 61 cm thick shield.

In order to get an initial estimate of the effect of burnup on k_{eff} , a core loaded uniformly with fresh TRU fuel was depleted using ORIGIN¹⁷ for 3000 days. The multiplication constant varied from 1.035 to 0.736 due to the depletion of TRU and buildup of fission products, providing an indication of the range of k-variation that must be compensated by the neutron source.

The tritium self-sufficiency calculation was based on a scenario in which the GCFTR-3 operates with 600 day burn cycles, separated by a 60 day shutdown for fuel shuffling. In each cycle 58.5 kg of tritium is produced. This amount is sufficient to refuel the neutron source during that cycle and to ensure that after 60 days decay enough tritium remains to operate for one week in the next cycle.

The values for the Doppler temperature coefficient of reactivity were calculated. KENO predicted a value of -0.795 pcm/K while EVENT predicted a value of -0.589 pcm/K. The option of including ^{238}U with TRU to reduce the burnup reactivity decrement is being considered. The Doppler coefficient varies linearly with ^{238}U content. With approximately 40% of the fuel ^{238}U , the Doppler coefficient is -130 pcm/K.

The reactivity insertion due to complete He coolant voiding was calculated to be -119 pcm.

Use of a Lithium Injection Module⁴⁰, located above or below the core, for emergency shut down was investigated. Pressurized lithium would be introduced into the core by the breaking of a temperature-sensitive seal.

A shield design based on (ODS steel, He, B_4C , HfC, Ir, WC, Cd) was analyzed with MCNP. In order for the magnets to be lifetime (30 EFPH) components, the maximum allowable fast (>0.1 MeV) neutron fluence at the location of the superconductor is 10^{19} n/cm², and the maximum allowable dose to the insulation is 10^9 rads. The predicted lifetime fast neutron fluence is 1.6×10^{18} n/cm² and the predicted dose to the insulation is 3.1×10^7 rads.

H. Fusion Neutron Source

A tokamak neutron source capable of producing 200 to 500 MW fusion power (7.9 to 17.6×10^{19} neutrons/s) was designed to satisfy the engineering and physics constraints⁴¹, with a major radius $R=3.75$ m and plasma radius $a=1.08$ m. A current of 8.3 would be needed at 200 MW, and a current of 10 MA would be needed at 500 MW. The 500 MW operation would require in kinetic-to-magnetic pressure ratio $\beta_N = 2.85$ and confinement enhancement $H = 1.06$. The operational spaces at 9 MA and 10 MA are shown in Figs. 7 and 8.

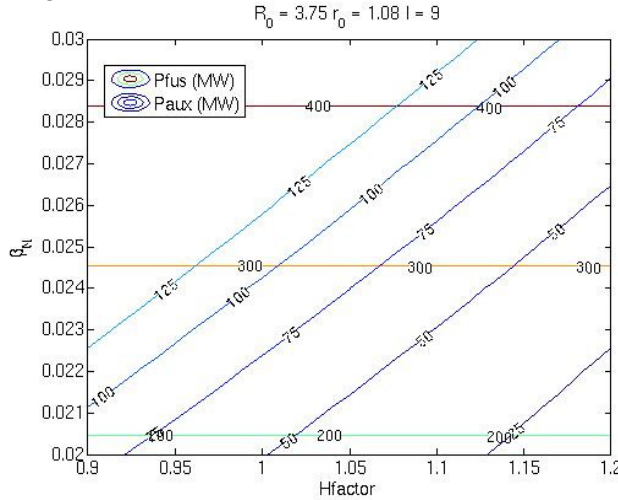


Figure 7: Fusion Power at I=9 MA.

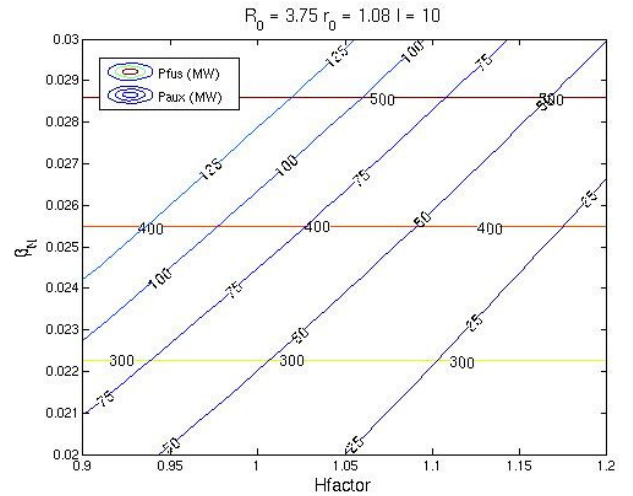


Figure 8: Fusion Power at I=10 MA.

Adaptation of the ITER divertor²⁷ (shown in Figs. 9 and 10) from water to helium to handle heat flux loads in the range of 0.5 to 2 MW/m² could be sustained with a total mass flow rate of 89 to 222 kg/s, requiring a total pumping power of 0.5 MW and 10 MW.

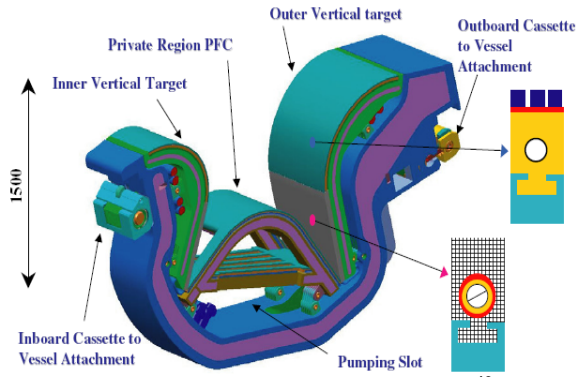


Figure 9: Divertor Cassette⁴²

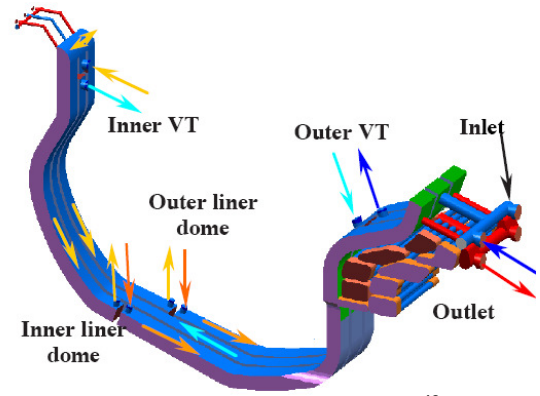


Fig. 10: Divertor coolant flow⁴³

Adaptation of the ITER Lower Hybrid system²⁷ provides a maximum simultaneous power output of 100 MW through six .773 x .773 m 20 MW LH ports, with an effective power density of approximately 33 MW/m² through each port. The LH Heating & Current Drive system for GCFTR is indicated in Fig. 11 and Table 7.

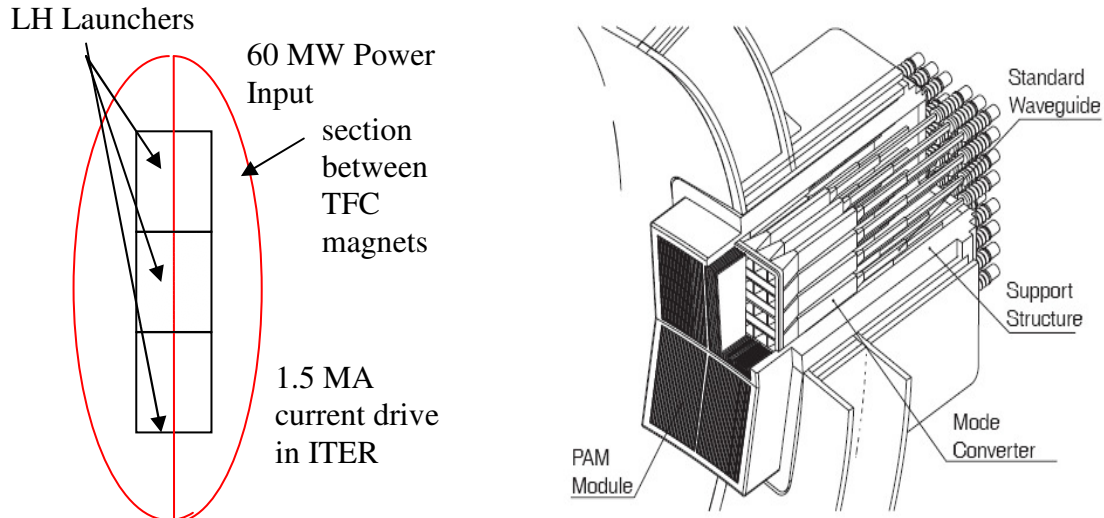


Figure 11: (a) LH Port Geometry⁴⁴, (b) LH Launcher⁴⁴.

Table 7: GCFTR-3 H&CD properties^{44,45,46}.

Property	GCFTR-3	ITER
Bootstrap Current	2.5 MA	~7.5 MA
Fractional Bootstrap Current	25%	~50%
Plasma Current	10 MA	15 MA
Maximum Simultaneous H&CD power	100 MW	110 MW
Total H&CD Capacity	120 MW	130 MW
Number of Port Plugs	6	10*
Power Density	33 MW/m ²	9.2 MW/m ² **

* 4 equatorial, 3 upper, 3 NBI, ** Power density in generic 20MW port

Stress calculations confirmed that the ITER magnet system²⁷ could be adapted, within the ITER structural constraints, for the GCFTR with 10 MA current.

References

1. "GEN-IV International Forum: Nuclear Energy Systems for the Future", Web site <http://www.gif.inel.gov/>.
2. "Advanced Fuel Cycle Initiative", Web site <http://www.nuclear.gov/afci>.
3. GNEP
4. "First Phase P&T Systems Study: Status and Assessment Report on Actinide and Fission Product Partitioning and Transmutation", OECD/NEA, Paris (1999).
5. "Proc. 1st-5th NEA International Exchange Meetings", OECD/NEA, Paris (1990,92,94,96,98).
6. "Nuclear Wastes--Technologies for Separations and Transmutations", National Research Council, National Academy Press, Washington (1996).
7. W. M. Stacey, et al, "A Fusion Transmutation of Waste Reactor", Fusion Science and Technology, 41, 116-140 (2002); also "A fusion transmutation of waste reactor", Fusion Eng. Des., 63-64, 81 (2002).
8. W. M. Stacey, et al., "A Subcritical, Gas-Cooled Fast Transmutation Reactor with a Fusion Neutron Source", Nucl. Technol., 150, 162 (2005).
9. W. M. Stacey, et al., "A Sub-Critical, He-Cooled Fast Reactor for the Transmutation of Spent Nuclear Fuel", Nucl. Technol., (October, 2005).
10. W. M. Stacey, et al., "Sub-Critical Transmutation Reactors with Tokamak Fusion Neutron Sources", Fusion Sci. Technol., 47, 1210 (2005).
11. W. M. Stacey, et al., "Advances in the Sub-Critical, Gas-Cooled, Fast Reactor Concept", Nucl. Technol., submitted (2006).
12. E. A. Hoffman and W. M. Stacey, "Nuclear and fuel cycle analysis for a fusion transmutation of waste reactor", Fusion Engr. Des., 63-64, 87 (2002); also "Nuclear Design and Analysis of the Fusion Transmutation of Waste Reactor", Fusion Sci. Technol., 45, 51 (2004).
13. E. A. Hoffman and W. M. Stacey, "Comparative fuel cycle analysis of critical and sub-critical fast reactor transmutation systems", Nucl. Technol., **144**, 83 (2003).
14. A. N. Mauer, W. M. Stacey and J. Mandrekas, "A Superconducting Tokamak Fusion Transmutation of Waste Reactor", Fusion Sci. Technol., 45, 55 (2004).
15. J. W. Maddox and W. M. Stacey, "Fuel Cycle Analysis of a Sub-critical, Fast, He-Cooled Transmutation Reactor with a Fusion Neutron Source", Nuclear Technol., to be published (2006).
16. C. de Oliveira and A. Goddard, "EVENT-A Multidimensional Finite Element-Spherical Harmonics Radiation Transport Code," Proc. Int. Seminar 3-D Deterministic Radiation Transport Codes, Paris, France, Organization for Economic Cooperation and Development (1996).
17. "ORIGEN-S: SCALE System Module to Calculate Fuel Depletion, Actinide Transmutation, Fission Product Buildup and Decay, and Associated Radiation Source Terms," NUREG/CR-200, Rev. 7 (ORNL/NUREG/CSD-2/V2/R7) Oak Ridge National Laboratory (2004).
18. B. J. Toppel, "A User's Guide to the REBUS-3 Fuel Cycle Analysis Capability," ANL-83-2, Argonne National Lab (1983).
19. "DANTSYS: A Diffusion Accelerated Neutral particle Transport Code System," LA-12969-M Manual UC-705, Los Alamos National Laboratory (1997).
20. H. Henryson et al., "MC²-2: A Code to Calculate Fast Neutron Spectra and Multigroup Cross Sections," ANL-8144, Argonne National Laboratory (1976).
21. "Understanding NJOY", Los Alamos National Lab report LA-UR-00-1538 (2000).
22. J. Mandrekas and W. M. Stacey, "Evaluation of Different Control Methods for the Thermal Stability of ITER", Fusion Technol., 19, 57 (1991).
23. J.E. Cahalan and M. Eriksson, "Active and Passive Safety Control Performance in Sub-critical, Accelerator-Driven Nuclear Reactors", 3^d International Workshop on the Utilization and Reliability of High Power Proton Accelerators, Santa Fe NM, 2002.
24. M. Eriksson and J.E. Cahalan, "Inherent shutdown capabilities in accelerator-driven systems", Annals of Nuclear Energy 29, 1689 (2002).
25. W. M. Stacey, *Nuclear Reactor Physics*, Wiley-Interscience, New York (2001), chp 5 and 16.

26. W. van Rooijen, "Improving Fuel Cycle Design and Safety Characteristics of a Gas Cooled Fast Reactor", PhD Thesis, Delft Technical University, (2006).
27. ITER website www.iter.org.
28. R. N. HILL and H. S. KHAHIL, "Physics Studies for Sodium Cooled ATW Blanket", Argonne National Lab report ANL/RAE/CP-105355 (2001).
29. F. H. Southworth, et al., "The Next Generation Nuclear Plant (NGNP) Project", Proc. Global 2003 Conf., New Orleans, LA, November 16-20, 2003, American Nuclear Society CD-ROM (2003).
30. M. ZHOU, Georgia Tech, Personal communication, (2006).
31. T. YOSHITAKE, Y. ABE, N. AKASAKA, S. OHTSUKA, S. UKAI, AND A. KIMURA, "Ring-tensile properties of irradiated oxide dispersion strengthened ferritic/martensitic steel claddings," *J. Nucl. Mater.*, 329-333 **344** (2004).
32. G. Vandegrift, et al., "Lab-Scale Demonstration of the UREX+ Process." *Waste Management Conference*, Tucson, AZ February 29--March 4, 2004 (2004).
33. J. Law, et al., "Development and Demonstration of Solvent Extraction Processes for the Separation of Radionuclides from Acidic Radioactive Waste" *Waste Management* 19, 27 (1999).
34. M. Ozawa, et al., "A New Reprocessing System Composed of PUREX and TRUEX Processes for Total Separation of Long-Lived Radionuclides" *Fifth OECD/NEA Information Exchange Meeting on Actinide and Fission Product Partitioning and Transmutation*, SCK-CEN, Mol, Belgium; November 25-27, 1998 (1998).
35. E. Teughert, K. Haas, A. Van Heek, P. Kasten, "Distribution of the Decay Heat in Various Modular HTRs and Influence on Peak Fuel Temperatures," Energy Conversion Engineering Conference, Philadelphia, PA August 10-14, (1987).
36. M.S. Kazimi and N.E. Todreas, *Nuclear Systems I: Thermal Hydraulics Fundamentals*, pp 295-338, Hemisphere Publishing Corporation, New York (1990).
37. M.J. Moran and H.N. Shapiro, *Fundamentals of Engineering Thermodynamics*, pp 414-415, John Wiley & Sons, Inc, Hoboken, NJ (2004).
38. J. F. Briesmeister, Ed. "MCNP – A General Monte Carlo N-Particle Transport Code, Version 4B," Los Alamos National Laboratory, LA-12625-M (1997).
39. "KENO V.a: An Improved Monte Carlo Criticality Program," NUREG/CR-0200, Rev. 7, Vol.II, Section F11, ORNL/NUREG/CSD-2/R7 (2004).
40. M. Kambe and M. Uotani, "Design and Development of Fast Breeder Reactor Passive Reactivity Control Systems: LEM and LIM", *Nuclear Technology*, 122, 179-195 (1998).
41. W. M. Stacey, *Fusion Plasma Analysis*, Wiley-VCH, Berlin (1005), chp 19.
42. J. Schlosser, F. Escourbiac, M. Merola, *et al.*, *Nuclear Fusion* **45**, 512 (2005).
43. ITER Technical Basis, Section 2.4, Divertor.
44. ITER Technical Basis, Chap. 2.5 Additional Heating and Current Drive, G A0 FDR 101-07-13 R1.0 (2001).
45. Y. Sakamoto, et al., "Stationary High Confinement Plasmas with Large Bootstrap Current Fraction in JT-60U", EX/4-3.
46. "Technical Parameters" Web Site <http://www.iter.org/index.htm>.

Recent Publication on Fast Transmutation Reactors with Fusion Neutron Sources

1. W. M. Stacey, et al., "Advances in the Sub-Critical, Gas-Cooled, Fast Transmutation Reactor Concept", *Nuclear Technol.*, submitted (2006).
2. W. M. Stacey, et al., "Tokamak Neutron Source Requirements for Nuclear Applications", *Nucl. Fusion* (submitted 2006).

3. W. M. Stacey, et al., “Sub-Critical Transmutation Reactors with Tokamak Neutron Sources Based on ITER Physics and Technology”, Fusion Sci. Technol., submitted (2006).
4. J-P. Floyd, et al., “Tokamak Fusion Neutron Source for a Fast Transmutation Reactor”, Fusion Sci. Technol., submitted (2006); with others.

V. INVESTIGATION OF THE INFLUENCE OF DIFFERENT AUXILIARY HEATING METHODS ON THE DENSITY LIMIT IN TEXTOR (Paper NP1.00025 at APS-DPP 2006) Z. W. Friis--Georgia Tech, Y. Liang, H.R. Koslowski, A. Kramer-Flecken, G. Sergienko, O. Zimmermann, G. Bertschinger, K. Löwenbrück, R.C. Wolf--Institut für Plasmaphysik, Forschungszentrum Jülich, Association EURATOM-FZJ, Trilateral Euregio Cluster, Germany, www.fz-juelich.de/ipp, M. von Hellermann--FOM-Institute for Plasma Physics Rijnhuizen, Association EURATOM-FOM, The Netherlands, www.rijnh.nl

Abstract

The dependence of plasma rotation and heating power on the density limit for MARFE onset has been studied on TEXTOR using different mixtures of auxiliary heating methods (ICRH, co-, and ctr- NBI). The edge density limit in the plasma heated by NBI is two times larger than that observed in the plasma heated by ICRH ($P_{\text{NBI}} = P_{\text{ICRH}} = 1.3 \text{ MW}$). The dependence of the density limit with regard to NBI direction is not noticeable, which could be because variation of plasma edge rotation by NBI is one or two orders of magnitude lower than the ion sound speed. The experimental data indicates that the different heating methods change the distribution of the neutral particle flux, which plays an important role in determining the threshold for the MARFE onset.

A. Introduction

In a series of density limit discharges on the Tokamak TEXTOR, it was shown that the Greenwald number varies with auxiliary heating power by $P^{0.44}$ as illustrated in Fig. 1 [1]. However, in the same illustration, the edge density limit seems to plateau towards the upper heating levels.

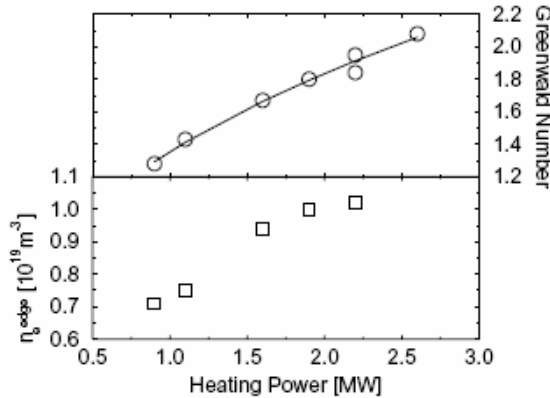


Figure 1: Dependence of Greenwald number on the heating power. The regression yields $P^{0.44}$. Dependence of the edge electron density ($a + 1 \text{ cm}$) on the heating power ($I_p = 230 \text{ kA}$).

In order to reach the power levels used in the experiment in Fig. 1, both co- and counter-neutral beam injections must be used in nearly equal parts. When the beam powers were balanced towards the upper heating limits of the device, the total momentum input should have been reduced. This would in-turn decrease the poloidal velocity in the edge [2].

From a different set of experiments, it has also been shown that the poloidal flow in the edge induced by the Dynamic Ergotic Divertor (DED) could “smooth” the distribution of the neutral particle recycle. The “smoothing” of the neutral particle flux helped to extend the MARFE density limit [3]. To test whether flow might have an effect on the MARFE density limit, a series of Rotation Scan Density Limit discharges has been carried out on the Tokamak TEXTOR [2]. TEXTOR was an ideal machine for this particular experiment given its size and the availability of both co- and counter- neutral beam injection.

B. Experimental Setup

To perform the Rotation Scan Density Limit discharges, all of the main plasma parameters (I_p , B , a , etc.) were kept constant. The total input power was maintained at 1.3 MW for each discharge varying only the method at which it was obtained in order to vary the total input momentum. To vary the momentum input, we used two methods. In the first method, only co and counter beam were used. The shot sequence started with pure co beam injection. In the next discharge, the co beam power was decreased slightly, while the counter beam was turned on to compensate. In the third shot, the co beam was decreased again, and the counter beam increased to match the co beam. We continued this for two more discharges, ending with pure counter beam and no co beam.

The second method used to vary the momentum input comprised of using a combination of co beam injection and ICRH. ICRH deposits very little momentum into the plasma, so it was thought that by keeping the total input power the same, but varying the amount of ICRH and co beam injection we could also vary the poloidal flow in the edge. Fig. 2 shows the experimental measurements of the toroidal flow in the edge for both sequences of discharges.

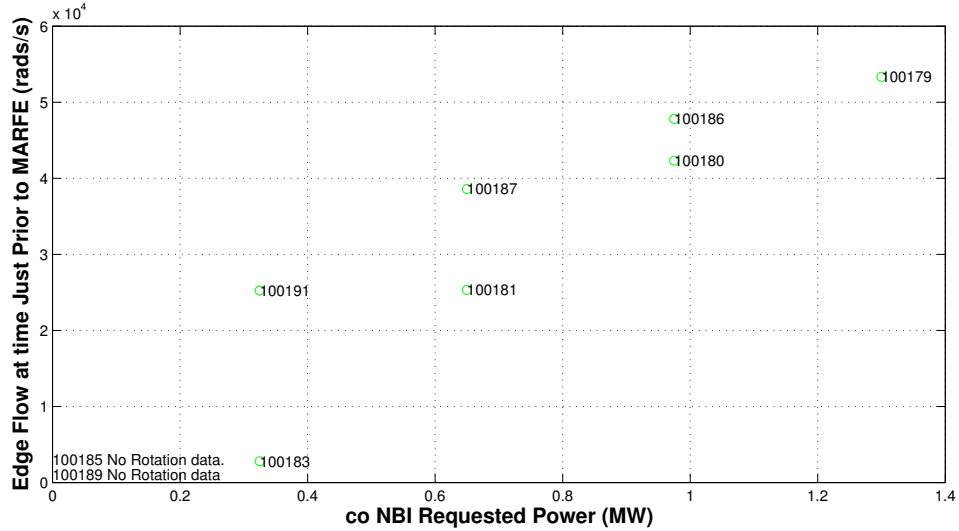


Figure 2: Toroidal Flow Measurements

As one can see, the toroidal rotation does indeed decrease as the co- beam power decreases. (The discharges that contain no co-NBI have no measurement for toroidal velocity as the diagnostic used to measure toroidal velocity requires the co- neutral beam injector). It should be noted that there was no diagnostic available to measure the poloidal velocity; however, we estimate that the poloidal velocities should be approximately an order of magnitude lower than above measured toroidal velocities.

As suggested earlier, it was postulated that enhanced poloidal flow in the plasma edge may “smooth” the neutral particle recycle. To see if this indeed happened for this experiment the maximum edge density limit at the edge was recorded at a time just prior to MARFE formation.

This was then compared with the ratio of the H_α line from the High Field Side (HFS) over the Low Field Side (LFS) at a time shortly after the heating scenario was set up.

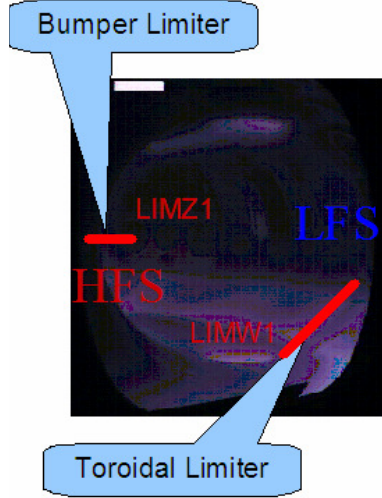


Figure 3: LIMZ1 measures the H_α signal over the HFS and LIMW1 measures the H_α signal just above the alt toroidal limiter.

The H_α signal is a measure of the amount of light coming from hydrogen undergoing an atomic transition. This signal is often proportional to the neutral particle flux in the region. A ratio of these signals from the HFS to the LFS is a “quick and dirty” way of estimating the distribution of the neutral particle flux in the edge. Because there is usually a much higher neutral particle flux just above the LFS due to the alt limiter, it is thought that an increase in the ratio illustrates a smoothing of the neutral particle flux.

C. Results

The comparison of the Edge Density Limit to the H_α ratios yielded some interesting results. The results do not conclusively show that the edge density is influenced by edge rotation; however, this could be due to the fact that the maximum edge velocity measured is at least an order of magnitude lower than the ion sound speed.

There are, however, significant differences in the edge density limit versus the methods of heating used. Figures 4 are plots of the ratio of the H_α signal versus the co beam input power on the left and the maximum edge density versus the co beam input power on the right.

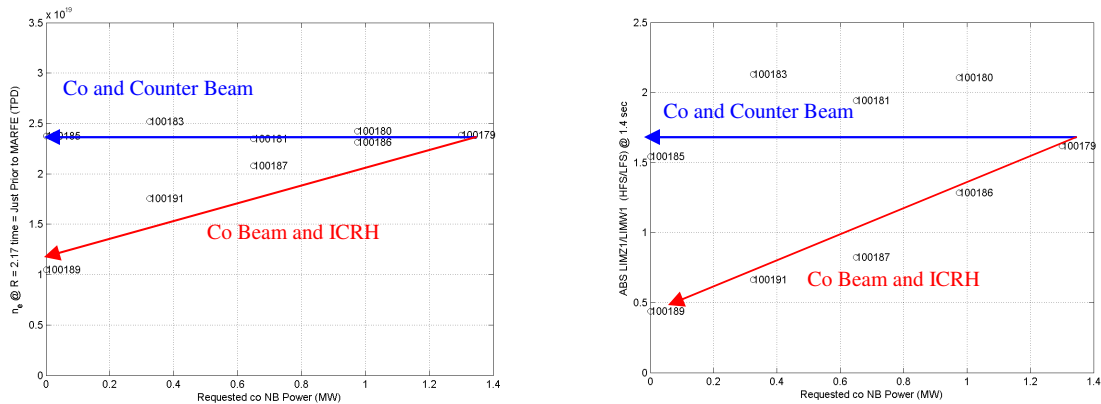


Figure 4: Maximum Edge Electron Density (m⁻³) versus Co NBI (MW) beam power on the Left, H_α ratio versus Co NBI Power (MW) on the right.

Surprisingly, the two plots seem to synch up with one another. Discharges with the higher edge density limit had a higher ratio of the H_α signals, which would imply that the neutral particle flux in the edge may be more distributed.

A similar pattern was found later the same day in a power scan series of discharges. In Fig. 5, the main plasma parameters were the same as the rotation scan. The only difference in the discharges was that the power was increased in each discharge using a several different types of heating methods. Three separate trends can clearly be seen.

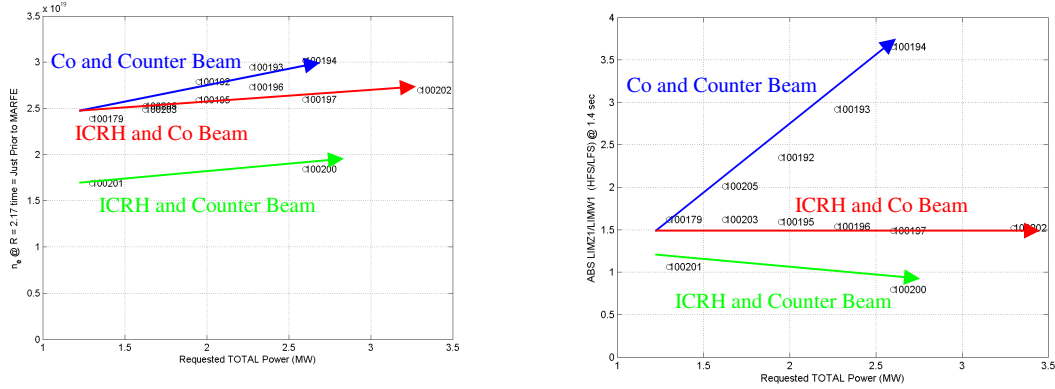


Figure 5: The left side is the maximum edge electron density (m^{-3}) versus the requested total power (MW), and the right side is the ratio of the H-alpha signals versus the requested total power (MW).

The left side of Fig. 5 shows similar results to the rotation scan. In predominately co- and counter- beam heated discharges, the maximum edge density is higher than discharges heated with a mixture of ICRH and co- beam injection. The right side of Fig.5 displays how the maximum edge density synchs with the ratio of the H_α signals.

D. Conclusion

The preliminary conclusions that may be drawn from these series of experiments is that there is a significant difference in the way the neutral particle flux is distributed versus the method of auxiliary heating, and the difference in the neutral particle flux distribution coincides with the maximum recorded density in the edge. The reasons for this are being examined. So far, the prevailing theory is that near the ICRH antenna (which is located just above the alt-limiter), there is a localized cooling source. The cooling source could increase the amount of neutral particles and initiate conditions for MARFE onset [4, 5]. A detailed neutrals analysis is currently being done using the GTNEUT code. With this analysis, a clearer picture of what is going on should become available.

References

1. Rapp, J., et al., *Density limits in TEXTOR-94 auxiliary heated discharges*. Nucl. Fusion, 1999. **39**(6): p. 765-776.
2. Friis, Z.W., Liang, Y., *Does the plasma flow effect the density limit in Tokamaks?* 2005, Institut für Plasmaphysik, Forschungszentrum Jülich, GmbH.
3. Liang, Y., et al., *Influence of the Dynamic Ergodic Divertor on the Density Limit in TEXTOR*. PRL, 2005. **94**: p. 105003.
4. Guirlet, R., et al. *MARFE and Density Limit Detachment with the Tore Supra Actively Cooled Limiter*. in *29th EPS Conference on Plasma Phys. and Contr. Fusion Montreux*. 2002.
5. Tokar, M.Z., et al., *Localized recycling as a trigger of MARFE*. J. Nucl. Mater., 1999. **266-269**: p. 958-963.